Nanostructured Ni-Co Alloys with Tailorable Grain Size and Twin Density

B.Y.C. WU, P.J. FERREIRA, and C.A. SCHUH

We present an experimental approach to systematically produce nanostructures with various grain sizes and twin densities in the Ni-Co binary system. Using electrodeposition with various applied current densities and organic additive contents in the deposition bath, we synthesize nanostructured fcc and hcp solid solutions with a range of compositions. Due to the low stacking fault energy (SFE) of these alloys, growth twins are readily formed during deposition, and by adjusting the deposition conditions, a range of twin boundary densities is possible. The resulting nanostructured alloys cannot be described by a single characteristic length scale, but instead must be characterized in terms of (1) a true grain size pertaining to general high-angle grain boundaries and (2) an effective grain size that incorporates twin boundaries. Analysis of Hall–Petch strength scaling for these materials is complicated by their dual length scales, but the hardness trends found in Ni-80Co are found to be roughly in line with those seen in pure nanocrystalline nickel.

I. INTRODUCTION

BULK nanocrystalline materials are characterized by a large volume fraction of intercrystalline component, *i.e*, grain boundaries and triple junctions, and have been produced from various pure metals, alloys, and ceramics over the past two decades.[1–4] One of the superior properties these materials exhibit with respect to their microcrystalline counterparts is their extremely high strength or hardness. This high hardness is often explained by the Hall–Petch relationship,[5,6] which states that the hardness of a material increases with the reciprocal square root of grain size. However, it has also been observed that when the grain size is reduced below a critical value, materials no longer deform *via* the same mechanisms, and their strength or hardness no longer follows the Hall–Petch relationship.[7–12] From molecular dynamics (MD) simulations, several authors have found that below a critical grain size dislocation behavior begins to change character, giving way to processes dominated by grain boundary activity, including grain boundary shearing.[8,13–22] An interesting aspect of this transition is that near or below the critical grain size, deformation may become controlled by the nucleation and motion of partial dislocations, which leads to the formation of stacking faults and, potentially, deformation twinning.

The first suggestion that stacking faults may be important in the deformation of nanocrystalline metals was provided by MD simulations, in which partial dislocations were observed nucleating from the grain boundaries of nanocrystalline fcc metals.[8,13,16,21] For example, Yamakov and co-workers[15,16,23] as well as Van Swygenhoven and co-workers[24] have explicitly discussed the effect of stacking fault energy on the nucleation and propagation of partial dislocations in simulated nanocrystalline solids. Froseth and co-workers[25] have studied the effect of pre-existing twins upon the deformation mechanism of nanocrystalline Al. They reported that in defect-free nanocrystalline Al twinning was not a dominant deformation mechanism, but in the presence of pre-existing twins, the deformation mechanism could change substantially and twin boundary migration could emerge as the controlling mechanism.

Some experimental work has also addressed the issue of twins and stacking faults in nanocrystalline materials. For example, Lu and co-workers[26,27] observed that fine-grained samples of copper with a high density of nanoscale growth twin boundaries showed a unique combination of strength, strain hardening, and ductility. Chen *et al*.,[28] as well as Liao *et al*.,[29,30] have experimentally explored deformation twinning and stacking fault formation in nanocrystalline Al. Moreover, Liao *et al*.[31] showed that at a very slow strain rate, twinning became a major deformation mechanism in nanocrystalline Cu during high-pressure torsion. In addition to these works on nanocrystalline metals, research on other classes of nanoscale materials have also focused upon similar twin-related themes. For example, in thin films and nanolaminates, growth twins have been found to significantly contribute to hardness.[32–36] All of these experimental results for nanostructured metals are generally in line with prior work at coarser microstructural length scales; most studies have concluded that twin boundaries are similar to general high-angle grain boundaries in terms of their ability to disrupt dislocation motion.[37–42]

Although there remain many questions as to the specific roles of stacking faults and twins on deformation of nanostructured materials, all of the preceding results point to an important contribution from these defects. In this context, it would be very desirable to have experimental control over, *e.g*., stacking fault energy (SFE) and twin density in bulk nanostructured alloys. Both of these parameters can, in principle, be controlled in electrodeposited metals, where changes in the temperature, chemistry, and current characteristics of the deposition process can lead to changes in twin density, and variation of the deposit composition can produce a range of SFEs.[26,27,43,44] It is the purpose of this work to explore the possibility of such nanostructure control for alloys in the binary Ni-Co system. Because of the complete solid solubility

B.Y.C. WU, Graduate Student, and C.A. SCHUH, Salapatas Assistant Professor of Metallurgy, are with the Department of Materials Science and Engineering, Massachusetts Institute of Technology, Cambridge, MA 02139. Contact e-mail: schuh@mit.edu P.J. FERREIRA, Assistant Professor, is with the Materials Science and Engineering Program, University of Texas at Austin, Austin, TX 78712.

Manuscript submitted September 24, 2004.

of this system and the low SFE of Co, nanocrystalline alloys in this system can be tailored to exhibit a wide variety of structures from fcc to hcp, with a range of effective SFEs, and with various twin densities. For this purpose, we employ the well-established techniques of electrodeposition,[45] which allow the production of many alloys based on Ni and Co, and which also allow variation in the density of twin boundaries if the processing conditions are properly controlled.

II. EXPERIMENTAL

We have prepared nanostructured Ni-Co alloys through a process of aqueous electrodeposition; prior work using similar techniques to produce Ni-Co alloys is reviewed in Reference 45. The main components of our electrodeposition system were a power supply (Dynatronix, model PDPR40-50-100, Dynatronix, Amery, WI) and an electrolyte-containing beaker, which was immersed in a large digitally controlled thermal bath with the temperature set to 35 °C. The cathode was a 6.5 cm^2 commercial purity titanium plate (Alfa Aesar, Ward Hill, MA) mounted such that only one mirror-finish surface of the plate was exposed to the deposition solution; titanium was used because we found that the deposited films could be easily peeled off the substrate and the substrate reused. Two parallel anodes consisting of 99.995 pct Co and 99.995 pct Ni were used, and the bath was constantly stirred by a magnetic stirrer. The base composition of the bath is given in Table I; the typical volume of deionized water we used here was 1.0 L. The pH of the bath was measured by a digital pH meter (VWR model SB2, VWR International, Westchester, PA) that was frequently calibrated. For all of the experiments to follow, we have used pulsed current in order to reduce stress in the films and to promote nucleation of grains; the pulse on-time and off-time were each set to 5 ms (duty cycle = 50 pct). Further details on the deposition system and the procedures used here are available in Reference 46.

With the general system setup and baseline chemical bath described previously, two series of experiments were conducted in which one variable was adjusted independently of the others.

(1) *Current density*: For the first series of experiments, the bath composition listed in Table I was used, and the average current density was varied over the range from 1.7 to 23.7 A/dm^2. These experiments produced films in the composition range 12 to 68 at. pct Co (balance Ni).
(2) *Saccharin addition*: For this second series of experiments, different levels of saccharin were added to the bath, keeping all other conditions constant, with J_m = 5.1 A/dm^2. The minimum nonzero saccharin level investigated in this series of experiments was 0.01 g/L, and the maximum 12 g/L, with 13 intermediate values also explored. For all of these depositions, the composition of the resulting films was 80 ± 3 at. pct Co, with the composition balance being Ni.

Table I. Baseline Chemical Composition of the Electrodeposition Bath Used in the Present Work

Chemical	Addition Amount (g/L)
$NiSO_4 \cdot 6H_2O$	30
$CoSO_4 \cdot 7H_2O$	30
$NiCl_2 \cdot 6H_2O$	15
H_3BO_3	15
NaCl	10

After deposition, each film was removed from the substrate and characterized in a variety of ways. Small sections from each film were mounted in cross section and mechanically polished. Scanning electron microscopy (LEO 438 VP, Carl Zeiss, SMT, Thornwood, NY) and energy-dispersive spectroscopy (EDS) were used on both the planar and polished cross-sectional surfaces of the films. The chemical analysis capability of EDS was sufficient for determining the Ni and Co content of the films to within ±2 pct, and for examining compositional gradients through the cross section. Select samples were also subjected to wet chemical composition analysis to verify the accuracy of the EDS measurements.

X-ray diffraction (Rigaku RU300 X-ray diffractometer (Rigaku, The Woodlands, TX) using Cu K_α radiation) was performed on each specimen for the purposes of (1) identifying the phases present and (2) estimating the grain size. In order to determine the grain size, the Scherrer formula was used, and the Cauchy–Gaussian assumption was applied to correct for instrumental peak broadening; as described in Reference 47, this method gives a close approximation to the mean grain size determined by transmission electron microscopy (TEM). For the line broadening analysis, the most prevalent reflection was always used. In fcc structures, this was the (220) reflection, and in hcp the $(11\bar{2}0)$ or (0002) peak. Although XRD–based methods are not recommended for grain size analysis of highly textured electrodeposits, most of the specimens produced here had very weak textures, as will be seen later. For a number of select deposits, observations of the alloy structure were made using a focused ion-beam microscope (FIB, from FEI, Inc., Hillsboro, OR) in backscatter imaging mode, or using TEM. The TEM specimens were prepared by dimpling and subsequent ion milling (at liquid nitrogen temperature), and were observed in a JEOL* 2010 FX transmission electron microscope operated at 200 keV.

*JEOL is a trademark of Japan Electron Optics Ltd., Tokyo.

Some of the films were subjected to microindentation by a Vicker's hardness tester (LECO, DM-400, LECO Corporation, St. Joseph, MI) with a load of 25 g. For this purpose, mounted and polished cross sections were used to avoid the compliance problem sometimes observed in indentation of films on substrates. These indentations were very small (~5 μm wide) compared to the typical thickness of the deposits (~100 μm). A minimum of ten indentations were performed on each specimen, and the average hardness values are reported here.

III. CHEMICAL AND PHASE COMPOSITION OF THE DEPOSITS

Figure 1(a) illustrates that the Ni content of the deposits is dependent upon the average applied current density. It is apparent that most current densities led to Co-rich depositions, and only high currents favored the deposition of Ni, despite the fact that Ni is nobler than Co. This phenomenon is often termed

"anomalous deposition" and has been observed previously in the Ni-Co system.[48,49] For each of the deposited films, EDS analysis on the cross section verified that the composition was homogeneous, with no gradients through the film thickness. Accordingly, the reported values of composition are averages taken from two-dimensional scans across the entire cross section of the film. Finally, the impurity content of several typical films was analyzed using wet chemical methods. The only significant values so measured were for carbon and sulfur impurities, and were obtained from depositions prepared with heavy saccharin additions to the bath (10 g/L). Even in this extreme case, the impurity levels were only 160 ppm for carbon and 520 ppm for sulfur.

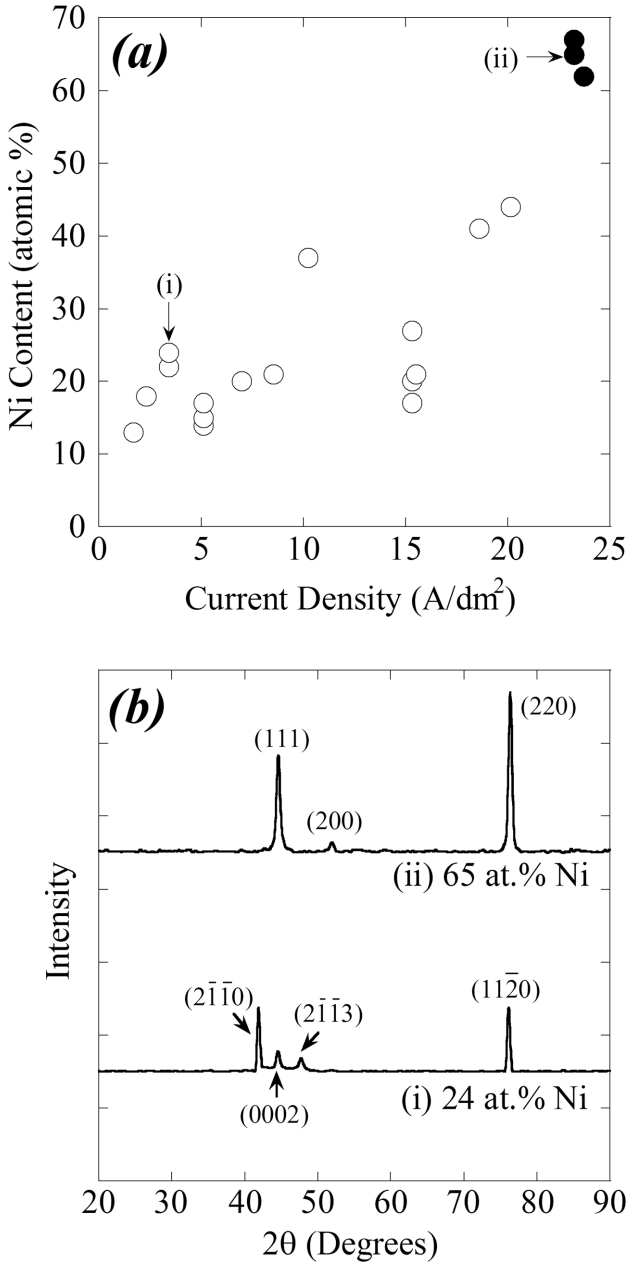

Fig. 1—Chemical and phase composition of the electrodeposited Ni-Co alloys, including (*a*) the effect of current density on the Ni content of the deposits, and (*b*) the resulting effect of Ni content on the crystal structure of the deposit, as seen in XRD patterns. The specimens labeled (i) and (ii) represent typical hcp and fcc structures, respectively, produced in the present work.

Typical X-ray diffraction (XRD) patterns are shown for representative, Ni-rich and Co-rich deposits in Figure 1(b). For Ni contents above 65 at. pct, all of the peaks could be indexed with fcc reflections, suggesting a single-phase solid solution. This result is in line with expectations, because pure Ni is fcc in equilibrium, and can dissolve substantial quantities of Co (up to ~60 pct at room temperature). As the Ni content decreases in favor of Co, Figure 1(b) reveals a shift to an hcp structure, again indicating a single-phase solid solution structure. The deposits investigated here did not exhibit dual-phase structures to within the resolution of XRD pattern analysis for the compositions studied, although such structures may be possible under other conditions.

IV. NANOSTRUCTURE OF THE DEPOSITS

The preceding results illustrate that a wide variety of alloy compositions can be electrodeposited in the Ni-Co system, ranging from Ni-rich fcc solid solutions of relatively high SFE, to Co-rich hcp solid solutions of nominally low SFE. In this section, we examine the structure of these alloys in some detail, focusing upon (1) grain size and (2) growth twin density. We begin with a brief discussion of Ni-rich (fcc) specimens, for comparison with the existing literature on Ni nanocrystals. Later, we more extensively examine hcp Co-rich alloys, and explore means of tailoring the nanostructure through changes in the deposition conditions.

A. *Ni-Rich Deposits*

Nickel is one of the most studied metals in nanocrystalline form, and there are numerous published TEM micrographs of electrodeposited specimens.[10,11,50–53] The typical grain structure of such materials may vary from columnar to equiaxed, but in none of the articles cited above is there a high density of growth twins in pure nanocrystalline Ni. The Ni-rich alloys plated in this work offer a striking contrast to this picture. Figure 2 is a TEM micrograph of a typical Ni-rich (Ni-35Co) deposit, where an abundance of nanoscale twins are present

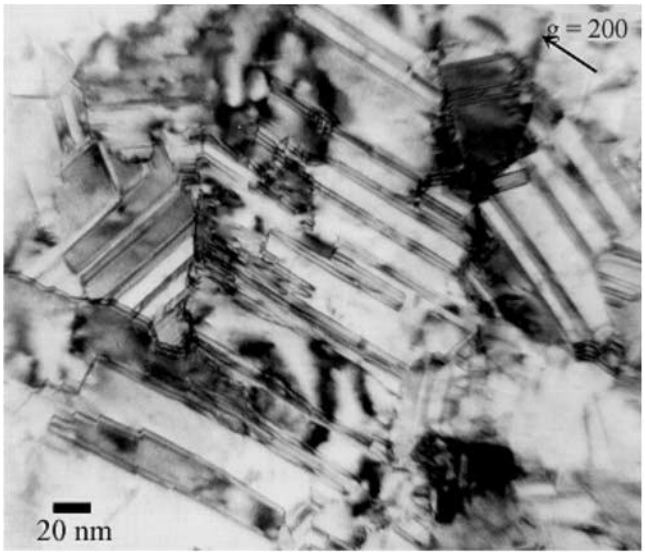

Fig. 2—A typical TEM bright-field image of a Ni-rich fcc alloy produced in the present work (Ni-35Co). The beam direction B = [011].

in the interior of each grain. The nominal grain size, defined by the random high-angle grain boundaries, is approximately 200 nm in this specimen, but it is clear that a second, finer characteristic length scale may also be defined. If the twin boundaries are taken into account, the effective grain size, given by the linear intercept method, is approximately 50 nm. This unique dual-scale structure will be discussed at more length in later sections, with reference to Co-rich deposits.

Although in-depth discussion of these Ni-rich specimens will be deferred to future work, it is interesting to observe that Co alloying additions are very effective in tailoring the nanostructure of fcc Ni. Whereas some kind of organic nucleation agent (*e.g.*, saccharin) is usually required to electrodeposit nanocrystalline Ni,[11,52] the addition of cobalt leads to a very different nanostructure where a high twin density is favored. Presumably, this significant nanostructural change is due to the reduced SFE of Ni-Co solid solution relative to pure Ni, which correlates with a low enthalpy penalty for the presence of twin boundaries.

B. *Co-Rich Deposits*

In typical studies of electrodeposited nanocrystals, it is common to tailor the grain size using organic additives (*e.g.*, saccharin) to the deposition bath. To our knowledge, however, there has not been a systematic study as to how saccharin influences the characteristic nanostructural length scales in a system such as Co-Ni, where growth twins are an important structural constituent. In what follows, we present a systematic study on the role of saccharin additions upon the nanostructure of hcp Ni-80Co alloys. As a baseline for this set of experiments, the structure of a typical Ni-80Co alloy is illustrated by the FIB micrograph of Figure 3. This specimen was produced without any saccharin addition to the deposition bath, at an average current density of 5.1 A/dm^2. The average grain size obtained by the linear intercept method in Figure 3 was approximately 800 nm. In contrast to the Ni-rich specimens described previously, the apparent twin density is rather low, at least within the resolution of the FIB imaging capability. As we will see in what follows, the grain size and twin density in this system are both significantly influenced by the addition of saccharin to the deposition bath.

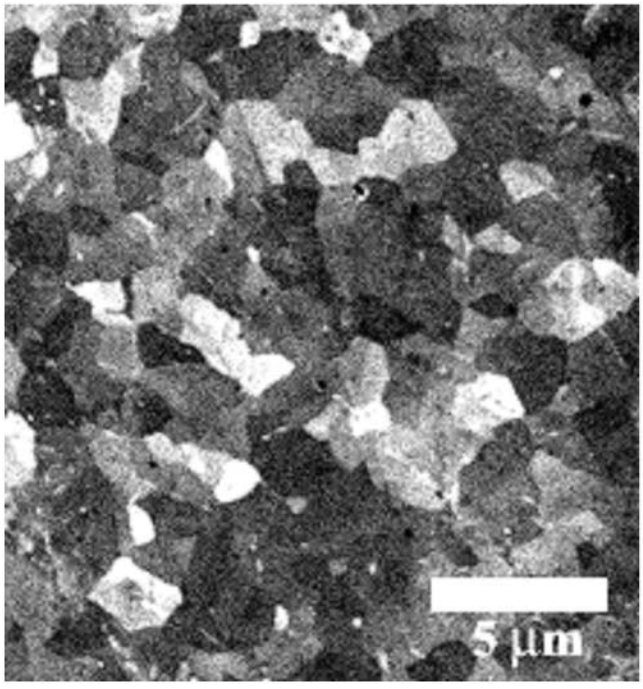

Fig. 3—A focused ion-beam micrograph (in backscatter mode) of a typical Co-rich hcp alloy electrodeposited without saccharin additions to the deposition bath (Ni-80Co). The true grain size seen here is ~0.8 μm and is the coarsest observed in the present work.

C. *Saccharin Additions for Nanostructure Control*

As described in Section II, various Ni-80Co alloys were deposited, with saccharine additions in the range 0.01 to 12 g/L. As has been seen in other electrodeposited systems,[54–56] saccharin had a clear effect upon the brightness of the deposited Ni-Co alloys. Specimens deposited without saccharin appeared dull and dark gray, while the addition of saccharin made the sample surface shiny. This transition in surface finish was obvious even when as little as 0.04 g/L of saccharin was added during deposition, and correlated with a shift in surface morphology, as seen in the SEM micrographs of Figure 4. The Ni-Co specimens deposited from a saccharin-free bath, shown in Figure 4(a), had visible pyramidal islands on the surface; this type of morphology persisted at a saccharin level of 0.02 g/L (Figure 4(b)) but essentially disappeared when 0.04 g/L of saccharin was added (Figure 4(c)). The colonylike morphology seen in Figure 4(c) was also suppressed when the saccharin level was greater than or equal to 0.5 g/L, giving way to a very flat and shiny surface. Figure 4(d) is an SEM surface micrograph of a deposit with 2.0 g/L of saccharin observed at the maximum magnification of the microscope. At this and all lower magnifications, the surface was devoid of topographical features.

Concurrent with the surface topography changes was a shift in the deposition texture of Ni-80Co, as shown in the XRD patterns of Figure 4(e). At or below the 0.02 g/L saccharin level, there was a clear $(11\bar{2}0)$ texture seen through the very strong reflection at $2\theta \approx 76$ deg. There was a sharp texture transition when 0.04 g/L of saccharin was added to the solution, with the strong $(11\bar{2}0)$ peak essentially disappearing in favor of a slight (0002) texture. These changes in preferred orientation are similar to prior observations in pure electrodeposited Co.[57]

Figure 5(a) illustrates the effect of finite saccharin levels on the XRD grain size of the Ni-Co alloys; it should be noted that these values are *effective grain sizes* that include the nanoscale twin density as well as the general high-angle grain boundaries. As expected, saccharin generally acted to refine the grain structure of electrodeposits. It was observed in this work that only 0.02 g/L of saccharin was needed to reduce the XRD grain size to 30 nm, and 0.04 g/L of saccharin was able to further reduce the grain size to below 20 nm; grain sizes below 20 nm were maintained with further saccharin addition. A similar trend has also been observed in the literature for other electrodeposited metals. For example, during the deposition of pure Ni, El-Sherik and co-workers found that initially the grain size decreased rapidly with increasing saccharin additions before reaching a plateau at saccharin concentration of 5 g/L; increasing the saccharin concentration from 5 to 10 g/L had little effect on grain size reduc-

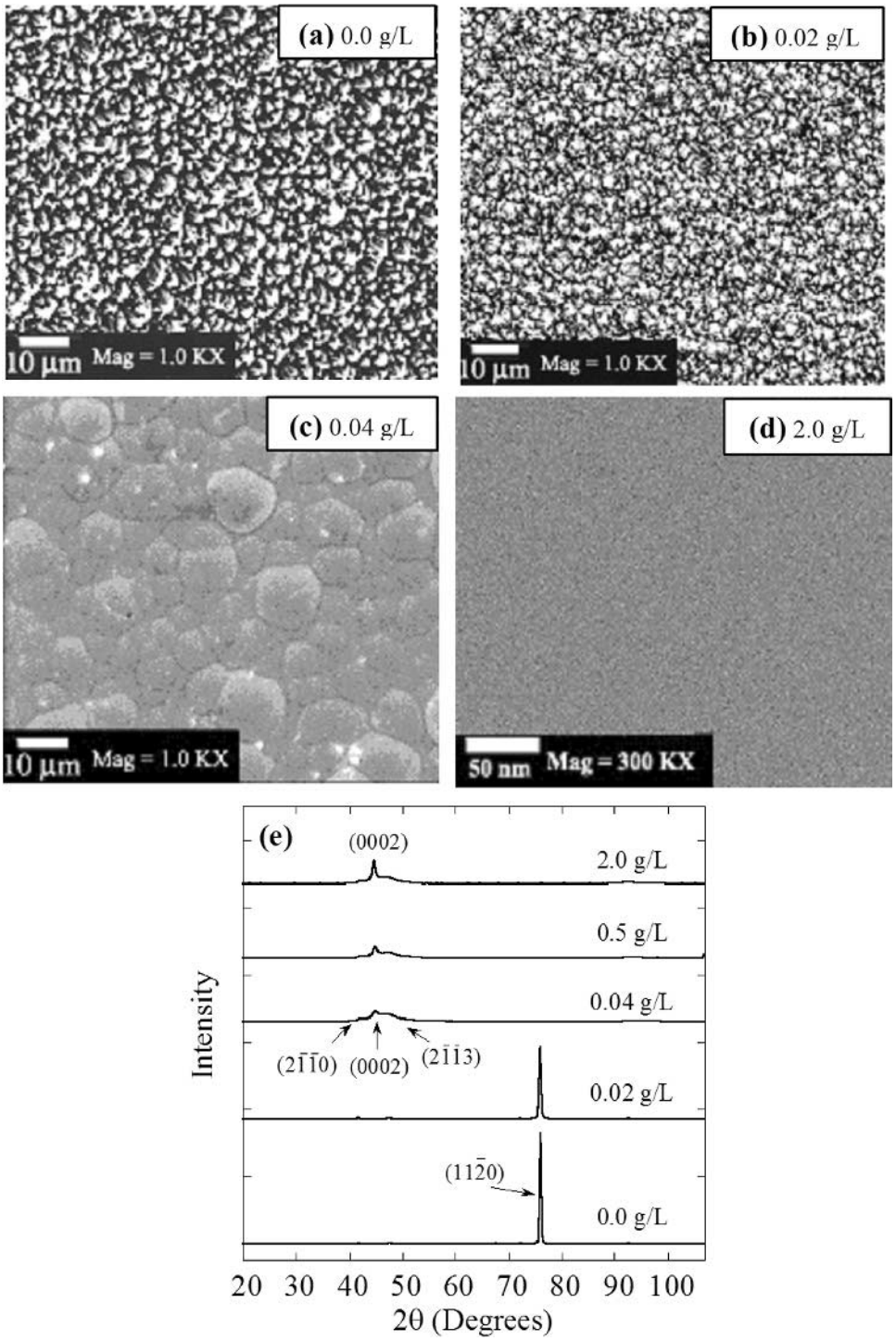

Fig. 4—The effect of saccharin addition on the topography and texture of electrodeposited Ni-80Co hcp alloys, seen through (*a*) through (*d*) SEM micrographs of the film surface and (*e*) corresponding XRD patterns. The saccharin level used in these depositions was (a) 0.0 g/L, (b) 0.02 g/L, (c) 0.04 g/L, and (d) 2.0 g/L.

tion.[52] The data of these authors are plotted in Figure 5(a) for comparison with the present data.

Although saccharin is seen to refine the grain size in both pure Ni and Ni-80Co in Figure 5(a), the trend for Ni-80Co is considerably more complex than for pure Ni, exhibiting a minimum XRD grain size at ~0.05 g/L saccharin and increasing slightly thereafter; the same data are replotted on a semilog scale in Figure 5(b) to better observe this unusual trend. Since the principal difference between nanocrystalline Ni and Ni-Co lies in the presence *vs* absence of growth twins, it is reasonable to expect that the different behaviors seen in Figure 5 may be attributed to twin-related effects. In what follows, we explore the details of the nanostructure of these alloys through TEM investigation.

We begin with a specimen deposited using 0.05 g/L of saccharin in the bath, which gives the minimum XRD grain

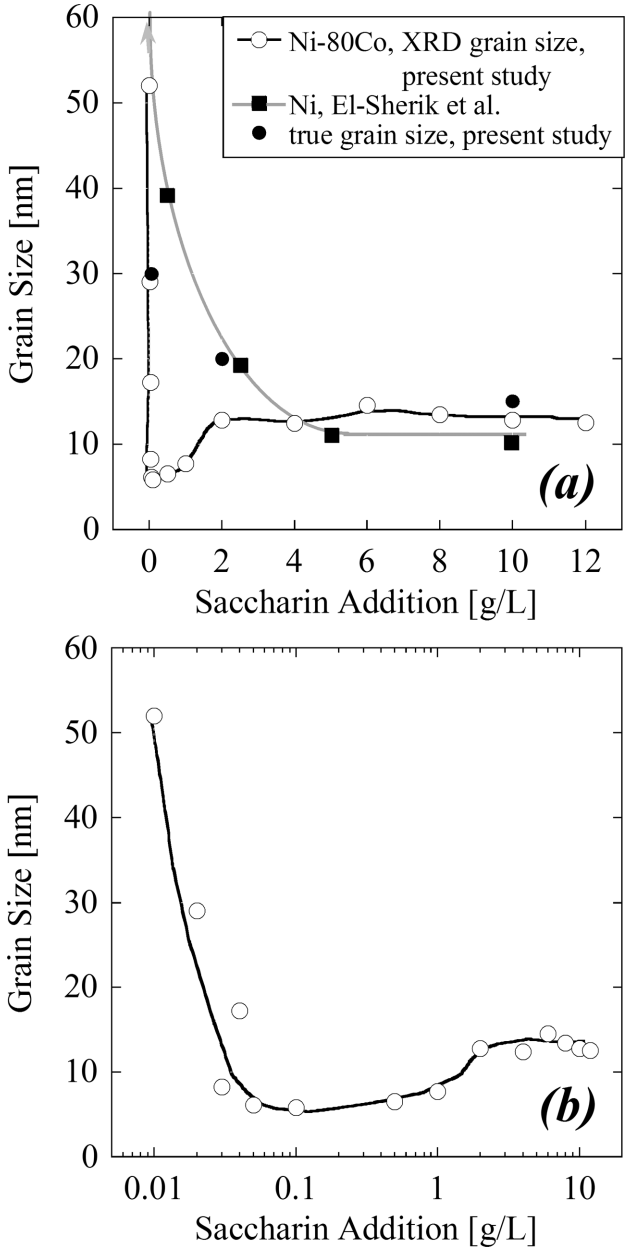

Fig. 5—The effect of saccharin addition on the characteristic length scales of electrodeposited metals. The effective XRD grain size of Ni-80Co alloys from the present work is compared with those obtained for pure Ni from El-Sherik *et al.*[52] Also shown are the measured values of true grain size for some of the present Ni-80Co alloys, defined by the network of general high-angle grain boundaries and measured from TEM micrographs. The solid lines are presented to better illustrate trends.

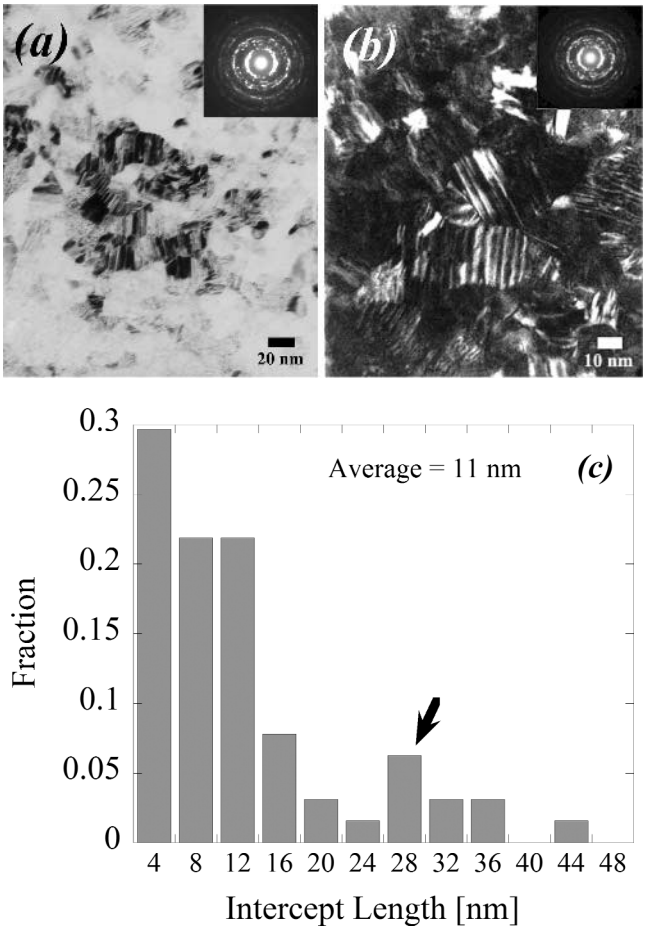

Fig. 6—Typical TEM micrographs of a Ni-80Co specimen deposited with 0.05 g/L of saccharine added to the deposition bath. Image (a) is a bright-field image, while (b) is a dark-field image; both show grains of ~30-nm size, containing a high density of nanoscale twins. The electron diffraction ring patterns of the imaged domains are also shown, revealing the small grain sizes obtained. The plot in (c) illustrates the distribution of linear intercept lengths obtained from TEM images of this specimen. The large fraction of intercept lengths below 12 nm is attributed to the finely spaced twin boundaries, while the low, secondary peak in the distribution at ~30 nm (noted by the arrow) is reflective of the true grain size.

size obtained in this study, ~6 nm, as shown in Figure 5. A heavily twinned structure, present as a result of the low stacking fault energy of Co, is evident in the TEM images in Figure 6. The electron diffraction pattern shown in the inset attests to a reasonably weak texture, which is consistent with the XRD results shown previously in Figure 4. Neglecting the many growth twins, we find that the "true" grain size of this specimen is approximately 30 nm. When the twin boundaries are included, a more interesting picture emerges, as illustrated in Figure 6(c). Here, a distribution of random linear intercept lengths is reported, based on manual measurements obtained from TEM images. The most significant feature of this distribution is the primary broad peak in the 4- to 12-nm range, which corresponds with the spread of twin boundary spacings observed in these specimens. However, as indicated by the arrow in Figure 6(c), a lower second mode of the distribution can also be seen at larger scales (near 30 nm), and this peak corresponds to the true grain size of the specimen. The dominance of the twin spacing peak relative to the true grain size peak is a consequence of the linear intercept approach used here; the true grain size is only infrequently measured when the measurement line falls parallel to the twin boundaries traversing a grain. When averaged, the linear intercept measurement gives a small characteristic grain size of ≈11 nm, which compares reasonably with the XRD grain size of ~6 nm and which is clearly dominated by the high density of nanotwins.

Figure 7 shows bright- and dark-field TEM images as well as the electron diffraction pattern for a Ni-Co specimen deposited with 2.0 g/L of saccharin. Figure 7(c) gives the

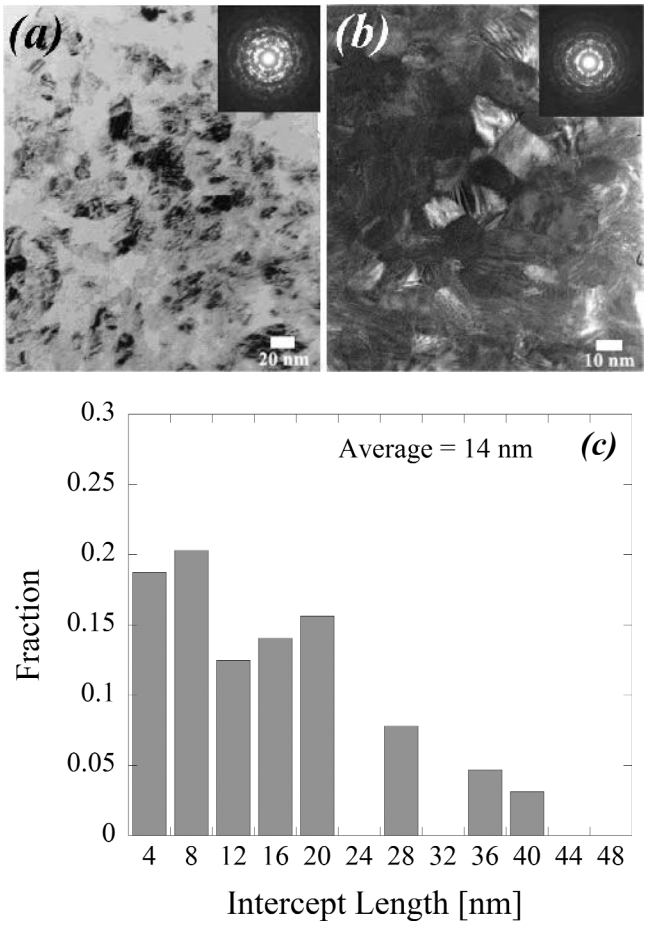

Fig. 7—TEM micrographs for Ni-80Co deposited with 2.0 g/L saccharin addition, including (*a*) bright-field and (*b*) dark-field images at the same magnifications used in Fig. 6. Here, we see nanocrystalline grains of ~20 nm as well as nanoscale twins, although the twin density is somewhat lower than observed in Fig. 6 with lower saccharin content in the deposition bath. (*c*) A plot illustrating the distribution of linear intercept lengths, where both the true grain size ~20 nm and the smaller nanotwin spacing <10 nm can be seen.

distribution of linear intercept lengths for this specimen, on the same axes used earlier in Figure 6(c). The distribution in the present case again exhibits a bimodal character with peaks near 8 and 20 nm, corresponding to the two characteristic length scales of the specimen. In this case, the density of twins is significantly suppressed as compared to the specimen examined earlier, which is easily seen through the different primary peak heights in Figures 6(c) and 7(c). As a consequence of the lower twin density in the specimen of Figure 7, the peak for the true grain size (~20 nm in Figure 7(c)) is much more pronounced. When the linear intercept data are averaged for the specimen in Figure 7 (inclusive of the twin boundaries), one can identify an effective grain size of about 14 nm, close to the XRD grain size of 13 nm. Finally, with a higher saccharin addition of 10.0 g/L, the Ni-Co specimen shown in Figure 8 looks quite like that shown in Figure 7 for a saccharin concentration of 2.0 g/L, which is reasonable given the structural changes associated with the saccharin addition plateau for additions above ~2.0 g/L (Figure 5).

The preceding results all give a consistent picture of electrodeposited Co-Ni alloys, which, in general, exhibit two distinct characteristic microstructural length scales.

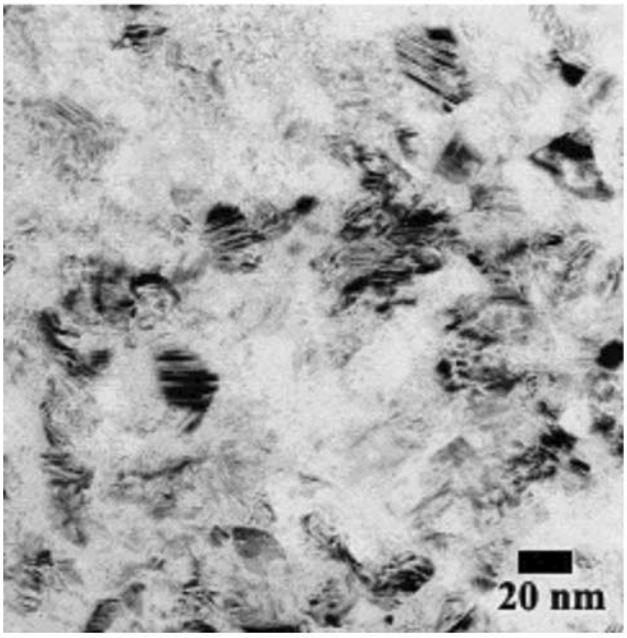

Fig. 8—A typical bright-field TEM micrograph of Ni-80Co deposited with 10.0 g/L of saccharin; the structure is quite similar to that observed with 2.0 g/L saccharin (Fig. 7(a)).

(1) The true grain size is defined by the network of general high-angle grain boundaries, and is found to decline from the micron range to about 15 nm as saccharin is added to the bath. The trend of this decline is in line with prior literature for, *e.g.*, pure Ni,[52] as illustrated in Figure 5 by the solid circular data points taken from our TEM observations. As described earlier, this refinement is usually attributed to enhanced grain nucleation, promoted by the interaction of saccharin with surface sites on the growing deposit.
(2) In contrast to the true grain size, the grain size measured by XRD is consistently finer, being influenced by the density of growth twins. The variation of twin density with saccharin content is more complicated than is the trend in true grain size, and is likely responsible for the unusual form of the XRD grain size curve seen in Figure 5. The TEM results suggest that higher saccharin concentrations in the bath suppress the growth of twins in the structure; this is evident from the specimens shown in Figs. 6 and 7 (deposited with 0.05 and 2.0 g/L saccharin, respectively), which have similar true grain sizes but quite different twin densities. It is not entirely clear why saccharin additions should suppress twin growth in these electrodeposits, but it may be associated with internal stress in the films; saccharin is known to relieve stresses in growing deposits, which gives rise to the surface morphology changes seen in Figure 4. It seems possible that with lower internal stress levels, the formation of growth twins (*via* dislocation-based mechanisms) could be significantly suppressed.

The complex trend of the "effective" XRD grain size with saccharin level seen in Figure 5 can be understood in terms of these two effects. Whereas saccharin leads to refinement of the true grain size, it promotes an increase in the average twin spacing (a decrease in twin density). The former

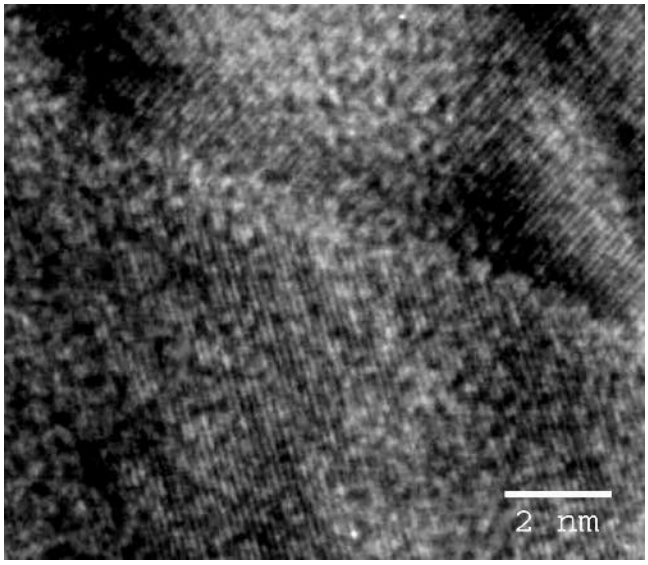

Fig. 9—A high-resolution TEM image of Ni-80Co (the same specimen shown in Fig. 8), focusing on a general grain boundary. The presence of lattice fringes up to the boundary suggests that there is no amorphous film at the boundaries in this alloy.

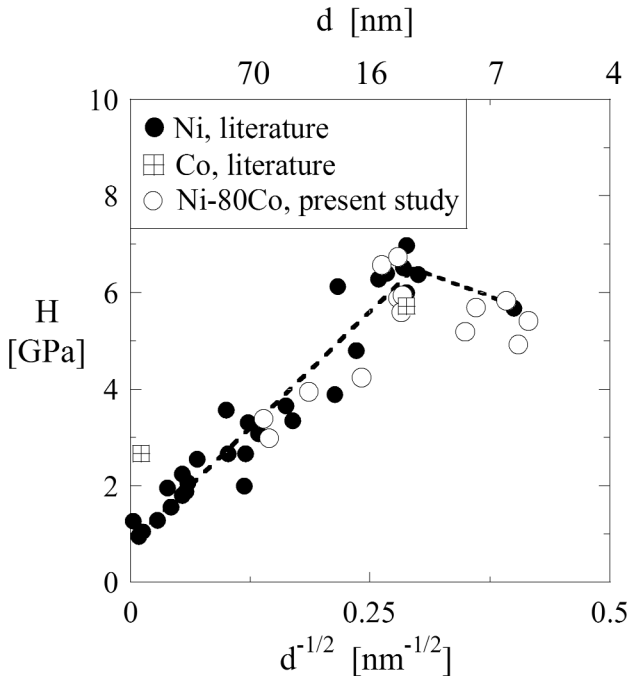

Fig. 10—Vicker's microhardness (H) plotted in Hall–Petch fashion, using the effective XRD grain size, d, as the dominant length scale. Also plotted are literature data for pure Ni[10,11,61–63] and pure Co.[57] The dashed trend lines are present for illustrative purposes only.

effect is responsible for the quick decline of the XRD grain size with the initial saccharin addition, while the latter is responsible for the subsequent minimum and subtle increase at higher saccharin levels.

To conclude this section, we comment briefly on the structure of grain boundaries in these Ni-80Co alloys. Figure 9 is a high-resolution TEM image of one of the specimens described previously (deposited with 10.0 g/L of saccharin), and provides a clear illustration of a typical random grain boundary in these materials. Whereas there have been some suggestions of amorphous regions near grain boundaries in other nanocrystalline metals (*e.g.*, the discussion in Reference 2), here we see that lattice fringes can be observed right up to the boundary from either side, indicating that there is no amorphous film at the grain boundary.

V. ROLE OF GRAIN BOUNDARY CHARACTER ON HARDNESS TRENDS

From the preceding discussion, it is clear that the nanostructure of the present Ni-Co alloys is quite different from typical nanostructured Ni, by virtue of the very high density of twins (and potentially of other stacking fault–related defects as well). With two nominally different structural length scales in these specimens, it is questionable whether scaling relationships such as, *e.g.*, the Hall–Petch relation, can be legitimately applied to these nanostructured Ni-Co alloys. As described in Section I, there is a growing interest in nanotwinned materials[25,26,27] and in dual-scale nanostructured materials in general,[58,59,60] where such issues are under active discussion. Accordingly, we will briefly explore the microhardness trends seen in our Ni-Co specimens in this section. It is important to note that these preliminary data provide no first-hand mechanistic insight into the deformation of nanostructured Ni-Co; such issues will be the domain of some of our future research. Furthermore, for simplicity, we will only discuss specimens of the same nominal composition, Ni-80Co; the only differences from specimen to specimen are in the nanostructure, which was manipulated as described earlier through saccharin additions to the electrodeposition bath.

The literature studies reviewed earlier are all in general agreement that twin boundaries impede dislocation motion in roughly the same way as general high-angle grain boundaries. Therefore, for relatively large grain sizes in the Hall–Petch strengthening regime, we might expect that the important length scale that governs strength is the effective (XRD) grain size, which incorporates all high-angle boundaries, general and twin alike. Accordingly, we have used the XRD grain size, d, to compile the Hall–Petch plot shown in Figure 10, which shows the Vicker's microhardness (H) as a function of $d^{1/2}$. For comparison with the present data, we have also included data from nominally pure Ni[10,11,61–63] and Co.[57]

At grain sizes above ~15 nm (to the left of Figure 10), we see that all of the data from the present study (Ni-80Co), as well as from prior literature on pure Ni and Co, fall into a reasonably common trend that follows the expected Hall–Petch scaling. This result confirms the expectations developed previously, and supports the notion that twin boundaries are effective Hall–Petch strengtheners. Given that Ni and Ni-80Co are metals of different crystal structure (fcc and hcp, respectively), the agreement between the Hall–Petch strengthening trends in Figure 10 is surprisingly good. What is perhaps even more surprising is that the Ni-80Co specimens also exhibit an apparent Hall–Petch breakdown over the same range of grain sizes (below about 15 nm) and hardness values ($H_{max} \approx 7$ GPa) that pure Ni does. Although the use of XRD grain size may be appropriate for large grain sizes where strength is controlled by dislocation-boundary interactions, it is almost certainly not appropriate to use this length scale to characterize grain size

below the Hall–Petch breakdown, where different deformation mechanisms operate. Accordingly, the agreement between the Ni and Ni-80Co data at fine grain sizes (<15 nm) in Figure 10 is most likely fortuitous. In what follows, we discuss the apparent Hall–Petch breakdown in Figure 10, and speculate about the implications of a high twin density on deformation mechanisms in nanostructured metals.

One possible interpretation of the data in Figure 10 is that because the hardness data are in close agreement, the mechanism of Hall–Petch breakdown is the same in both Ni and Ni-80Co. For example, if one imagines the critical grain size for the breakdown to be that at which a dislocation pileup can no longer be sustained within a grain, then the analysis of Nieh and Wadsworth[7] anticipates

$$d_c = \frac{3\mu\mathbf{b}}{\pi(1 - \nu)H} \qquad [1]$$

where d_c is the critical grain size, μ is the shear modulus, **b** is the magnitude of the Burger's vector, ν is the Poisson's ratio, and H is the hardness of the metal. In the case of Ni, Co, and Ni-Co alloys, the values of μ, **b**, and ν are all virtually identical from one composition to the next, and Figure 10 shows that in the Hall–Petch regime, where Eq. [1] holds, their approximate hardness values, H, are as well. Therefore, according to Eq. [1], predicated on the basis of the dislocation pileup analysis alone, one expects no significant difference in the critical grain size at which dislocation pileups are no longer sustainable (which is of the order of 10 nm for Ni and Co both). However, this kind of analysis does not consider the *mechanistic* transition that is required for Hall–Petch breakdown to occur; usually, the breakdown has been associated with the onset of interfacially dominated deformation mechanisms, including intergranular diffusion and grain boundary sliding. If one accepts the agreement between data sets at fine grain sizes (<15 nm) in Figure 10 as evidence that these mechanisms occur in the same way in both Ni and Ni-80Co, then it would follow that twin and general grain boundaries are equally prone to diffusional creep or sliding. It seems relatively unlikely that this is indeed the case, since it is known that twins and other low-Σ coincidence boundaries are resistant to sliding and diffusional creep as compared with general high-angle boundaries.[64–66]

A second (and far more realistic) possible interpretation for the data in Figure 10 is that the numerical agreement between the data below ~15 nm in Figure 10 is merely fortuitous; although an *apparent* Hall–Petch breakdown is observed for both materials, one may argue that their very different nanostructures would require very different breakdown mechanisms. For example, one can imagine that the Hall–Petch breakdown in Ni is associated with grain boundary diffusion or sliding, while that in Ni-80Co is related to twin boundary migration. The MD simulations of Froseth *et al.*[25] have shown that preexisting twin boundaries in nanocrystalline aluminum may accommodate strain by migrating, and it seems plausible that the transition from dislocation-dominated to twin-migration-dominated flow could occur at an effective grain size ~15 nm. Some indirect support for this interpretation is also provided by the work of Karimpoor *et al.*,[57] who studied the tensile ductility of electrodeposited pure cobalt. With a grain size ($d \approx 12$ nm) close to the apparent Hall–Petch breakdown we observed here ($d \sim 15$ nm), those authors observed unusually high tensile ductility of their specimens. They speculated that this ductility might have been associated with the emergence of twinning as a deformation mechanism at fine grain sizes. Twin boundary migration is a process accompanied by very little damage accumulation; if twin boundary migration could accommodate a large amount of strain before significant grain boundary deformation occurred, it is feasible that the onset of microvoiding and rupture could be suppressed in highly twinned nanocrystalline metals.

Since the present data provide only vague trends in a system with clear nanostructural complexities, it is impossible to draw firm conclusions as to the role of twin boundaries on strength. Nonetheless, the ability to produce nanocrystalline specimens with tailorable grain size and twin density offers a route to the experimental exploration of the role of twins on deformation physics, and presents a direction for future research.

VI. CONCLUSIONS

Nanocrystalline alloys were produced in the Ni-Co system using pulsed current electrodeposition. Applied current density was varied to effect different compositions ranging from Ni rich to Co rich, and both fcc and hcp crystal structures. Saccharin additions were also used to manipulate the structure of Ni-80Co deposits. The following main conclusions were reached.

1. For any composition from 30 to 90 at. pct Co, the alloys produced here exhibited complex dual-scale structures. One scale was defined by the general high-angle grain boundaries, and a second, finer scale was defined by the spacing between nanoscale growth twins, which were prevalent in all of the investigated specimens. The first length scale, the true grain size, ranged from ~20 nm to ~1 μm in the present alloys, while the second scale, the effective grain size, was often 50 nm or finer. It is interesting to observe that in the Ni-Co system, a nanometer-scale microstructure is developed for virtually any set of deposition conditions, owing to the development of nanoscale growth twins. This effect can be attributed to the low SFE of Ni-Co alloys, which reduces the energetic cost of twin boundaries.
2. In Ni-80Co alloys, saccharin additions led to the refinement of true grain size, in agreement with prior literature for electrodeposited Ni. However, saccharin also influenced the development of growth twins in the structure, apparently reducing the twin density.
3. The hardness of Ni-80Co specimens was found to follow very closely the trends observed in pure nanostructured Ni, with Hall–Petch strengthening dominating at larger grain sizes, followed by an apparent Hall–Petch breakdown for effective grain sizes below about 15 nm. Although the present data set is not sufficient to identify the mechanism responsible for Hall–Petch breakdown, it is unlikely that the same mechanism is at play in nanocrystalline Ni (with a relatively low twin density) and Ni-80Co (with a high twin density). It is proposed that twin boundary migration may be an important deformation mechanism in nanostructured Ni-80Co.

ACKNOWLEDGMENTS

This work was supported by the Defense University Research Initiative on NanoTechnology (DURINT), which is funded at MIT by the Office of Naval Research, Grant No. N00014-01-1-0808. The experimental involvement of Jin Ho An from the University of Texas at Austin, is gratefully acknowledged.

REFERENCES

1. J.R. Weertman, D. Farkas, K. Hemker, H. Kung, M. Mayo, R. Mitra, and H. Van Swygenhoven: *MRS Bull*., 1999, vol. 24, pp. 44-50.
2. K.S. Kumar, H. Van Swygenhoven, and S. Suresh: *Acta Mater*., 2003, vol. 51, pp. 5743-74.
3. C.C. Koch, D.G. Morris, K. Lu, and A. Inoue: *MRS Bull*., 1999, vol. 24, pp. 54-58.
4. H. Gleiter: *Progr. Mater. Sci*., 1989, vol. 33, pp. 223-315.
5. E.O. Hall: *Proc. Phys. Soc*., 1951, vol. B64, pp. 747-53.
6. N.J. Petch: *J. Iron Steel Inst*., 1953, vol. 174, pp. 25-28.
7. T.G. Nieh and J. Wadsworth: *Scripta Metall. Mater*., 1991, vol. 25, pp. 955-58.
8. J. Schiotz, F.D. DiTolla, and K.W. Jacobsen: *Nature*, 1998, vol. 391, pp. 561-63.
9. Y. Zhou, U. Erb, K.T. Aust, and G. Palumbo: *Scripta Mater*., 2003, vol. 48, pp. 825-30.
10. A.M. El-Sherik, U. Erb, G. Palumbo, and K.T. Aust: *Scripta Metall. Mater*., 1992, vol. 27, pp. 1185-88.
11. C.A. Schuh, T.G. Nieh, and T. Yamasaki: *Scripta Mater*., 2002, vol. 46, pp. 735-40.
12. C.A. Schuh, T.G. Nieh, and H. Iwasaki: *Acta Mater*., 2003, vol. 51, pp. 431-43.
13. J. Schiotz, T. Vegge, F.D. DiTolla, and K.W. Jacobsen: *Phys. Rev*., 1999, vol. B60, pp. 11971-11983.
14. V. Yamakov, D. Wolf, S.R. Phillpot, and H. Gleiter: *Acta Mater*., 2002, vol. 50, pp. 61-73.
15. V. Yamakov, D. Wolf, S.R. Phillpot, and H. Gleiter: *Acta Mater*., 2002, vol. 50, pp. 5005-20.
16. V. Yamakov, D. Wolf, M. Salazar, S.R. Phillpot, and H. Gleiter: *Acta Mater*., 2001, vol. 49, pp. 2713-22.
17. H. Van Swygenhoven and A. Caro: *Appl. Phys. Lett*., 1997, vol. 71, pp. 1652-54.
18. H. Van Swygenhoven, A. Caro, and D. Farkas: *Scripta Mater*., 2001, vol. 44, pp. 1513-16.
19. H. Van Swygenhoven, P.M. Derlet, and A. Hasnaoui: *Phys. Rev*., 2002, vol. B66, p. 024101.
20. H. Van Swygenhoven, M. Spaczer, and A. Caro: *Acta Mater*., 1999, vol. 47, pp. 3117-26.
21. H. Van Swygenhoven, M. Spaczer, A. Caro, and D. Farkas: *Phys. Rev*., 1999, vol. B60, pp. 22-25.
22. A.C. Lund, T.G. Nieh, and C.A. Schuh: *Phys. Rev. B*, 2004, vol. 69, 012101.
23. V. Yamakov, D. Wolf, S.R. Phillpot, and H. Gleiter: *Acta Mater*., 2003, vol. 51, pp. 4135-47.
24. H. Van Swygenhoven, P. Derlet, and A. Froseth: *Nature Mater*., 2004, vol. 3, p. 399.
25. A. Froseth, H. Van Swygenhoven, and P. Derlet: *Acta Mater*., 2004, vol. 52, pp. 2259-68.
26. L. Lu, Y. Shen, X. Chen, L. Qian, and K. Lu: *Science*, 2004, vol. 304, pp. 422-26.
27. E. Ma, Y.M. Wang, Q.H. Lu, M.L. Sui, L. Lu, and K. Lu: *Appl. Phys. Lett*., 2004, vol. 85, pp. 4932-34.
28. M. Chen, E. Ma, K.J. Hemker, H. Sheng, Y. Wang, and X. Cheng: *Science*, 2003, vol. 300, pp. 1275-77.
29. X.Z. Liao, F. Zhou, E.J. Lavernia, D.W. He, and Y.T. Zhu: *Appl. Phys. Lett*., 2003, vol. 83, pp. 5062-64.
30. X.Z. Liao, F. Zhou, E.J. Lavernia, S.G. Srinivasan, M.I. Baskes, D.W. He, and Y.T. Zhu: *Appl. Phys. Lett*., 2003, vol. 83, pp. 632-34.
31. X.Z. Liao, Y.H. Zhao, S.G. Srinivasan, Y.T. Zhu, R.Z. Valiev, and D.V. Gunderov: *Appl. Phys. Lett*., 2004, vol. 84, pp. 592-95.
32. X. Zhang, A. Misra, H. Wang, T.D. Shen, M. Nastasi, T.E. Mitchell, J.P. Hirth, R.G. Hoagland, and J.D. Embury: *Acta Mater*., 2004, vol. 52, pp. 995-1002.
33. X. Zhang, A. Misra, H. Wang, M. Nastasi, J.D. Embury, T.E. Mitchell, R.G. Hoagland, and J.P. Hirth: *Appl. Phys. Lett*., 2004, vol. 84, pp. 1096-98.
34. S.I. Rao and P.M. Hazzledine: *Phil. Mag. A*, 2000, vol. 80, pp. 2011-40.
35. A. Misra, J.P. Hirth, and H. Kung: *Phil. Mag. A*, 2002, vol. 82, pp. 2935-51.
36. R.G. Hoagland, T.E. Mitchell, J.P. Hirth, and H. Kung: *Phil. Mag. A*, 2002, vol. 82, pp. 643-64.
37. J.W. Christian and S. Mahajan: *Progr. Mater. Sci*, 1995, vol. 39, p. 1995.
38. M.A. Meyers and K.K. Chawla: *Mechanical Behavior of Materials*, Prentice-Hall, Inc., Elmsford, NJ, 1999.
39. L. Remy: *Metall. Trans. A*, 1981, vol. 12A, pp. 387-408.
40. W.J. Babyak and F.N. Rhines: *Trans. TMS*, 1960, vol. 21.
41. C.S. Pande, B.B. Rath, and M.A. Imam: Mater. Sci. Eng., 2004, vol. A367, pp. 171-75.
42. J.-Q. Su, M. Demura, and T. Hirano: *Acta Mater*., 2003, vol. 51, pp. 2505-15.
43. N.Y.C. Yang, T.J. Headley, J.J. Kelly, and J.M. Hruby: *Scripta Mater*., 2004, vol. 51, pp. 761-66.
44. F. Ebrahimi, Z. Ahmed, and H. Li: *Appl. Phys. Lett*., 2004, vol. 85, pp. 3749-51.
45. *Modern Electroplating*, M. Schlesinger and M. Paunovic, eds., John Wiley & Sons, New York, NY, 2000.
46. B. Wu: Master's Thesis, Massachusetts Institute of Technology, Cambridge, MA, 2004.
47. Z. Zhang, F. Zhou, and E.J. Lavernia: *Metall. Mater. Trans. A*, 2003, vol. 34A, pp. 1349-55.
48. A. Brenner: *Electrodeposition of Alloys—Principles and Practice*, Academic Press, New York, NY.
49. C. Fan and D.L. Piron: *Electrochimica Acta*, 1996, vol. 41, pp. 1713-19.
50. F. DallaTorre, H. Van Swygenhoven, and M. Victoria: *Acta Mater*., 2002, vol. 50, pp. 3957-70.
51. S. Van Petegem, F. Dalla Torre, D. Segers, and H. Van Swygenhoven: *Scripta Mater*., 2003, vol. 48, pp. 17-22.
52. A.M. El-Sherik and U. Erb: *J. Mater. Sci*., 1995, vol. 30, pp. 5743-49.
53. K.S. Kumar, S. Suresh, M.F. Chisholm, J.A. Horton, and P. Wang: *Acta Mater*., 2003, vol. 51, pp. 387-405.
54. J.K. Dennis and J.J. Fuggle: *Electroplat. Met. Fin*., 1967, vol. 30, p. 370.
55. A.M. El-Sherik: Ph.D. Thesis, Queen's University, Kingston, Canada, 1993.
56. R. Wei and H.C. Cook: *Plat. Surf. Fin*., 1962, vol. 109, p. 295.
57. A.A. Karimpoor, U. Erb, K.T. Aust, and G. Palumbo: *Scripta Mater.*, 2003, vol. 49, pp. 651-56.
58. Y. Wang, M. Chen, F. Zhou, and E. Ma: *Nature*, 2002, vol. 419, pp. 912-15.
59. D. Witkin, Z. Lee, R. Rodriguez, S. Nutt, and E.J. Lavernia: *Scripta Mater*., 2003, vol. 49, pp. 297-302.
60. G. He, J. Eckert, W. Loser, and L. Schultz: *Nature Mater*., 2003, vol. 2, pp. 33-37.
61. U. Erb: *Nanostr. Mater*., 1995, vol. 6, pp. 533-38.
62. F. Ebrahimi, G.R. Bourne, M.S. Kelly, and T.E. Matthews: *Nanostr. Mater*., 1999, vol. 11, pp. 343-50.
63. G.D. Hughes, S.D. Smith, C.S. Pande, H.R. Johnson, and R.W. Armstrong: *Scripta Metall*., 1986, vol. 20, pp. 93-97.
64. R.G. Hoagland and R.J. Kurtz: *Phil. Mag. A*, 2002, vol. 82, pp. 1073-92.
65. H. Kokawa, T. Watanabe, and S. Karashima: *Phil. Mag*., 1981, vol. A44, pp. 1239-54.
66. T. Watanabe: *Metall. Trans. A*, 1983, vol. 14A, pp. 531-45.